

# UC Riverside

## UC Riverside Previously Published Works

### Title

PIN2-mediated self-organizing transient auxin flow contributes to auxin maxima at the tip of Arabidopsis cotyledons.

### Permalink

<https://escholarship.org/uc/item/56p0m289>

### Journal

Nature Communications, 16(1)

### Authors

Pérez-Henríquez, Patricio

Nagawa, Shingo

Liu, Zhongchi

et al.

### Publication Date

2025-02-05

### DOI

10.1038/s41467-024-55480-8

Peer reviewed

# PIN2-mediated self-organizing transient auxin flow contributes to auxin maxima at the tip of *Arabidopsis* cotyledons

Received: 14 December 2022

Accepted: 9 December 2024

Published online: 05 February 2025

 Check for updates

Patricio Pérez-Henríquez <sup>1,2,10</sup>, Shingo Nagawa<sup>2</sup>, Zhongchi Liu<sup>3,4</sup>, Xue Pan<sup>1,5</sup>, Marta Michniewicz<sup>6,11</sup>, Wenxin Tang<sup>2</sup>, Carolyn Rasmussen <sup>1</sup>, Xiping Cui<sup>7</sup>, Jaimie Van Norman <sup>1,10</sup>, Lucia Strader <sup>6,8</sup> & Zhenbiao Yang <sup>1,2,3,4,9</sup> ✉

Directional auxin transport and formation of auxin maxima are critical for embryogenesis, organogenesis, pattern formation, and growth coordination in plants, but the mechanisms underpinning the initiation and establishment of these auxin dynamics are not fully understood. Here we show that a self-initiating and -terminating transient auxin flow along the marginal cells (MCs) contributes to the formation of an auxin maximum at the tip of *Arabidopsis* cotyledon that globally coordinates the interdigitation of puzzle-shaped pavement cells in the cotyledon epidermis. Prior to the interdigitation, indole butyric acid (IBA) is converted to indole acetic acid (IAA) to induce PIN2 accumulation and polarization in the marginal cells, leading to auxin flow toward and accumulation at the cotyledon tip. Once IAA levels at the cotyledon tip reaches a maximum, it activates pavement cell interdigitation as well as the accumulation of the IBA transporter TOB1 in MCs, which sequesters IBA to the vacuole and reduces IBA availability and IAA levels. The reduction of IAA levels results in PIN2 down-regulation and cessation of the auxin flow. Hence, our results elucidate a self-activating and self-terminating transient polar auxin transport system in cotyledons, contributing to the formation of localized auxin maxima that spatiotemporally coordinate pavement cell interdigitation.

Proper formation and morphogenesis of an organ requires not only the differentiation of cells and tissues, but also their coordinated growth in time and space, but the mechanisms for this coordination are mostly unexplored in multicellular organisms. The *Arabidopsis* cotyledon is an outstanding and trackable example of growth coordination and morphogenetic pattern formation towards the building

of an efficient light-capturing flat structure. The expanding epidermal layers of pavement cells (PCs) on both sides of the flat structure accommodate the expanding mesophyll cells. On the edges, a file of elongated cells called the marginal cells (MCs) surrounds the cotyledon. During cotyledon growth, PCs undergo a unique multi-polar expansion going from near cuboidal cells towards interdigitated

<sup>1</sup>Institute of Integrated Genome Biology, and Department of Botany and Plant Sciences, University of California, Riverside, CA 92521, USA. <sup>2</sup>Haixia Institute of Science and Technology, Fujian Agriculture and Forestry University, Fuzhou, Fujian, China. <sup>3</sup>Faculty of Synthetic Biology, Shenzhen University of Advanced Technology, Shenzhen, Guangdong, China. <sup>4</sup>The Key Laboratory of Quantitative Synthetic Biology, Shenzhen Institute of Advanced Technology, Chinese Academy of Sciences, Shenzhen, Guangdong, China. <sup>5</sup>Department of Biological Sciences, University of Toronto-Scarborough, Toronto, ON M1C1A4, Canada. <sup>6</sup>Department of Biology, Washington University, St. Louis, MO 63130, USA. <sup>7</sup>Department of Statistics, University of California, Riverside, CA 92521, USA. <sup>8</sup>Department of Biology, Duke University, Durham, NC 27708, USA. <sup>9</sup>Institute of Emerging Agricultural Technology, Shenzhen University of Advanced Technology, Shenzhen, Guangdong, China. <sup>10</sup>Present address: Department of Molecular, Cell and Developmental Biology, University of California, Los Angeles, CA 90095, USA. <sup>11</sup>Present address: Bayer Crop Science, 700 W Chesterfield Pkwy W, Chesterfield, MO 63017, USA. ✉e-mail: [zb.yang1@siat.ac.cn](mailto:zb.yang1@siat.ac.cn)

puzzle-shape cells<sup>1</sup>. The PC interdigitation event occurs with specific auxin signaling coordination throughout the cotyledon<sup>2</sup>. The small molecule phytohormone auxin acts as both a local and global signal to coordinate the PC interdigitation<sup>3–6</sup>. Local auxin activates cell surface signaling cascades that are independent of auxin-induced gene transcription and directly leads to PC interdigitation by regulating ROP GTPase-dependent cytoskeletal reorganization<sup>1,3,4,6,7</sup>. Auxin maxima and gradients peaking in a specific region of developing organs are a common feature in plants<sup>8,9</sup>. It serves as guidance for proper patterning, growth regulation, cell type differentiation and organogenesis<sup>10</sup>. Auxin accumulation at the cotyledon's tip is a widely reported observation<sup>11</sup>, however, the mechanism for the generation of this tip-high auxin remains unknown.

At the heart of auxin maximum/gradient formation is the integrated regulation of various mechanisms impacting cellular auxin levels<sup>12,13</sup>, including PIN-mediated polar auxin transport<sup>14–16</sup>, AUX1-mediated auxin influx<sup>17</sup>, ABC transporter mediated auxin efflux<sup>18,19</sup>, auxin biosynthesis and metabolism<sup>20–22</sup> and local subcellular sequestration of auxin or its precursors<sup>23–25</sup>. The absence of auxin transport and/or auxin biosynthesis can partially or completely disrupt the auxin gradients or maxima, proper patterning, and development. Thus, important developmental information is engraved in the spatial distribution of auxin<sup>8,26–28</sup>, but the nature of this information and the mechanism by which it controls the formation of specific auxin gradients/maxima are still enigmatic.

Auxin is synthesized predominantly from tryptophan through the intermediate INDOLE 3-PYRUVIC ACID (IPyA) in the TAA/YUCCA-regulated IPyA pathway<sup>29</sup>. Additionally, the INDOLE BUTYRIC ACID (IBA) pathway can locally boost auxin levels through the metabolic conversion of this auxin precursor into active auxin INDOLE ACETIC ACID (IAA). The IBA-to-IAA conversion pathway has been implicated in several developmental processes such as cotyledon expansion, organ size determination and lateral root formation<sup>25</sup>. It occurs through several enzymatic reactions in the peroxisome where the function of enoyl CoA-hydratase 2, ECH2, is a limiting step<sup>21</sup>. Cotyledons of the *ech2ibr1,3,10* quadruple mutant with impeded IBA-derived auxin exhibit severely impaired PC morphogenesis<sup>2,30</sup>. Cytoplasmic IBA levels can also be locally reduced by TOB1 (TRANSPORT OF IBA 1)-mediated vacuole transport<sup>24</sup>. Subcellular compartmentalization of IBA has been shown to regulate morphogenetic processes such as lateral root formation<sup>24</sup>.

Despite our extensive knowledge on the critical contribution of both auxin biosynthesis and polar transport to the formation of auxin maxima, it is unclear how these processes are regulated and coordinated to generate and maintain local accumulation of auxin. Here we address this question by using the unique cotyledon system, in which the auxin maximum at the cotyledon's tip is thought to guide its expansion. We showed that at the cotyledon edge, a file of elongated marginal cells accumulates polarly localized PIN2 forming a polar auxin transport system towards the tip. This auxin transport system is only transiently established via a self-activating and self-terminating mechanism to robustly coordinate PC interdigitation.

## Results

### PIN2-expressing margin cells coordinate pavement cell interdigitation

In developing organs, auxin maxima are formed via the polarized action of the plasma membrane (PM)-localized PIN-family auxin transporters<sup>8,15</sup>. Published transcriptional data reveals that PINs are induced during germination. Among all PINs, PIN2 shows the strongest expression in early imbibed seeds. (Supplementary Fig. 1a). Interestingly, we found PIN2-GFP<sup>31</sup> protein accumulated specifically in the lateral borders of early expanding cotyledons, forming a file of contiguous marginal cells (MCs) harboring PIN2 at their apical ends, resembling an “auxin transport pipeline” discharging at the cotyledon

tip (Fig. 1a and Supplementary Fig. 2b). The strong signal at the cotyledon tip does not reflect true PIN2-GFP but autofluorescence, as confirmed by spectral scanning microscopy (Supplementary Fig. 2a–c). Although we cannot exclude the role of other PINs, the apical localization of PIN2-GFP hints a role for PIN2 transporting auxin toward the tip of cotyledons along their marginal cells.

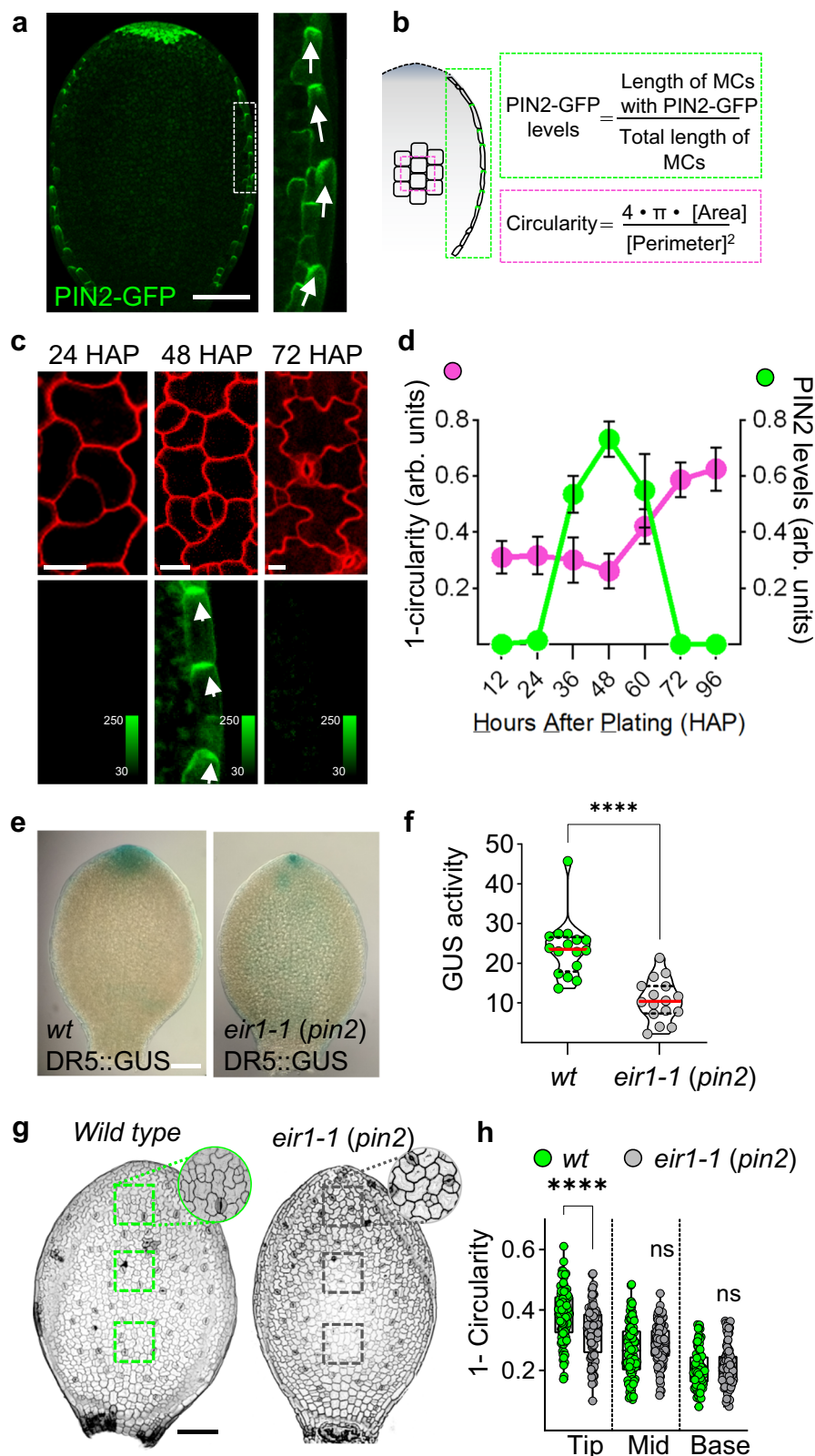
To further understand the correlation between PC interdigitation and PIN2-driven auxin transport, we analyzed the dynamics of PIN2-GFP accumulation in expanding cotyledons, from 12 to 96 Hours After Plating (HAP) (Fig. 1b). Strikingly, PIN2-GFP accumulation pattern in cotyledons was transient (Fig. 1c). Quantification revealed that PIN2 accumulation starts and consolidates before PC interdigitation is initiated (24–36 HAP) and is depleted once the interdigitation process is completed (72 HAP) (Fig. 1d). This suggests that PIN2-mediated auxin transport along MCs is involved in PC interdigitation presumably through contributing to the cotyledon's tip auxin maxima.

Importantly, the auxin transcriptional response marker *DR5::GUS* exhibited greatly reduced GUS signal at the cotyledon tip in the PIN2 loss of function mutant *eir1-1/pin2*<sup>32</sup>, compared to wild type (Fig. 1e). This reduced GUS signal was corroborated by the quantification of GUS activity in a fluorometric assay (Fig. 1f). Additionally, *pin2* showed less interdigitated and smaller PCs at the cotyledon tip (Fig. 1g, h and Supplementary Fig. 1c). Similar phenotypes were also observed in the insertional mutant allele *pin2-T*<sup>33</sup> (Supplementary Fig. 1d, e). These results imply that PIN2, which is specifically expressed in MCs, has a cell non-autonomous function in the promotion of PC interdigitation in cotyledons. To decipher the functional relevance of MCs in the regulation of PC interdigitation, we laser-ablated all MCs in a cotyledon prior to the initiation of PC interdigitation. At 24 h after ablation, the cotyledon displayed a strong inhibition of PC interdigitation, although its physiological status remained normal (Supplementary Fig. 2d–h). The laser ablation experiments hinted a role for PIN2-expressing MCs in the regulation of PC interdigitation. Altogether, low interdigitation in *pin2* cotyledon's tip, low auxin response in *pin2* cotyledon tips, consistent apical (towards tip) localization of PIN2 in consecutive MCs, and the importance of PIN2-expressing MCs revealed by laser ablation, suggest the importance of PIN2-mediated auxin transport along the cotyledon margins towards the tip for the formation of auxin maxima to coordinate PC interdigitation.

If MCs are indeed transporting auxin, we should be able to detect increased auxin levels in these cells after PIN2 is accumulated. We tested this by comparing nuclear auxin marker before and after PIN2-GFP accumulation (Fig. 2a, **24 vs 36 HAP**) in stable non-segregant lines containing both PIN2-GFP and the ratiometric auxin reporter R2D2<sup>34</sup>. R2D2 reports auxin-induced degradation of DII-Venus normalized by an auxin non-responsive version mDII protein (Fig. 2b). The nuclear quantification of R2D2 ratiometric index along MCs showed a ~50% increment after PIN2-GFP accumulation started (Fig. 2c), indicative of increased auxin levels along MCs. Taken together we conclude that a transient PIN2-based auxin flow through the cotyledons margin contributes to the tip auxin maximum and plays a role in coordinating the PC interdigitation process.

### Auxin positively feedback regulates polar auxin transport along the MCs

The transient nature of PIN2 accumulation presented an intriguing question: What are the underlying mechanisms behind initiation and termination of the PIN2 accumulation along MCs? The increased auxin levels together with PIN2-GFP polarization is consistent with the well-known effect of auxin regulating PIN expression<sup>35</sup>. Therefore, we supposed that auxin might positively regulate PIN2-mediated auxin transport along MCs. Indeed, we detected a dose-dependent rapid increase in the level of PIN2 localized to the apical plasma membrane after auxin treatments for 0.5 h, with a significant increase beginning at



100 nM IAA (Fig. 2d–f). PIN2 plasma membrane localization was also more polarized after auxin treatments (Supplementary Fig. 3d). Conversely, interruption of auxin transport by NPA treatment disrupted PIN2 polar localization (Supplementary Fig. 3a–c) and PC interdigitation (Supplementary Fig. 3e, f). Together these data suggest that an active “tip-wards” auxin transport along the MCs is initially organized by auxin itself.

#### IBA-derived auxin regulates PIN2 accumulation along MCs

To understand the biosynthetic origin of the auxin that flows along MCs, we explored the INDOLE 3-PYRUVIC ACID (IPyA) and INDOLE BUTYRIC ACID (IBA) pathways as possible sources of auxin. To this end, we used the presence or absence of key enzymes on each pathway as markers of their respective pathway activity. *ECH2p::YFP-ECH2*<sup>30</sup> and cytoplasmic *TAAIp::GFP-TAAI*<sup>11,36</sup> were used to mark IBA and IPyA

**Fig. 1 | PIN2 accumulation in MCs precedes and plays a role in coordinating PC morphogenesis.** **a** Polar PIN2-GFP in the apical side of marginal cells (MCs) of 48 Hours After Plating (HAP) *Arabidopsis* cotyledons. Image corresponds to a maximum intensity projection of a z-stack capturing all perceptible signal. Scale bar = 100  $\mu$ m. Zoom-in indicates the predicted direction of auxin flow with the white arrows from the base to the tip of the cotyledon. Note: Green signal at the cotyledon tip is not GFP, see Supplementary Fig. 2a. **b** Schematic of the areas analyzed on each cotyledon. **c, d** PIN2 accumulates transiently prior to PC morphogenesis. **c** Cell shapes visualized by PI (upper panel) staining at the adaxial side of cotyledons expressing PIN2-GFP (lower panel) and grown for 24, 48, 72 hours after plating (HAP). Shown are representative images captured in the center (PI) and in the border of the cotyledon (PIN2-GFP). Scale bar = 10  $\mu$ m. **d** Quantification of the interdigitation levels (magenta) and PIN2-GFP accumulation level (green) in 12 to 96 HAP cotyledons quantified as indicated in **b**. Interdigitation levels are expressed as 1-circularity, i.e., the greater the value, the greater the degree of interdigitation. Circularity is defined as  $4\pi \text{ area}/\text{perimeter}^2$ . PIN2 accumulation levels is quantified as the percentage in length of the border from base to tip that is expressing PIN2. Data is shown in arbitrary units (arb. units) as mean  $\pm$  SD.  $n = 12$  cotyledons from

different seedlings. **e, f** Reduced auxin transcriptional response in 48 HAP *eir1-1* (*pin2*) mutant. **e** Reduced *DR5::GUS* signal at the cotyledon's tip in *eir1-1* (*pin2*) compared to *wild type/wt*. Representative images are shown. The GUS signal was similarly displayed in 95% (19/20) and 84% (21/25) of the cotyledons assayed for *wt* and *eir1-1*, respectively. Scale bar = 100  $\mu$ m. **f** Reduced GUS activity in cotyledons *eir1-1* (*pin2*) measured by fluorometric quantification of 4-MU. GUS activity is shown as nanomolar units of 4-MU per sample. Unpaired two-tailed *t*-test. \*\*\*\*  $p$ -value < 0.0001.  $n = 16$  samples. Sample is defined as the 2 cotyledons in a seedling. **g, h** Loss-of-function mutant *eir1-1* (*pin2*) showed reduced interdigitation in pavement cells at the cotyledon tip. **g** Representative images of wild type and *eir1-1* (*pin2*) cotyledons. Boxes indicate areas to be quantified. Zoom-in shows the clear reduced interdigitation of pavement cells at the cotyledon's tip. Scale bar = 100  $\mu$ m. **h** Interdigitation level (1-circularity) in 3 areas of identical dimensions: tip, middle, and base for wild type *Col-0* (green dots) and PIN2 mutant allele *eir1-1* (*pin2*) (gray dots) in 60 HAP cotyledons.  $n = 90$  cells. Data was obtained from 5 different seedlings. Two-way ANOVA using Šidák's multiple comparisons test. \*\*\*\*  $p$ -value < 0.0001.

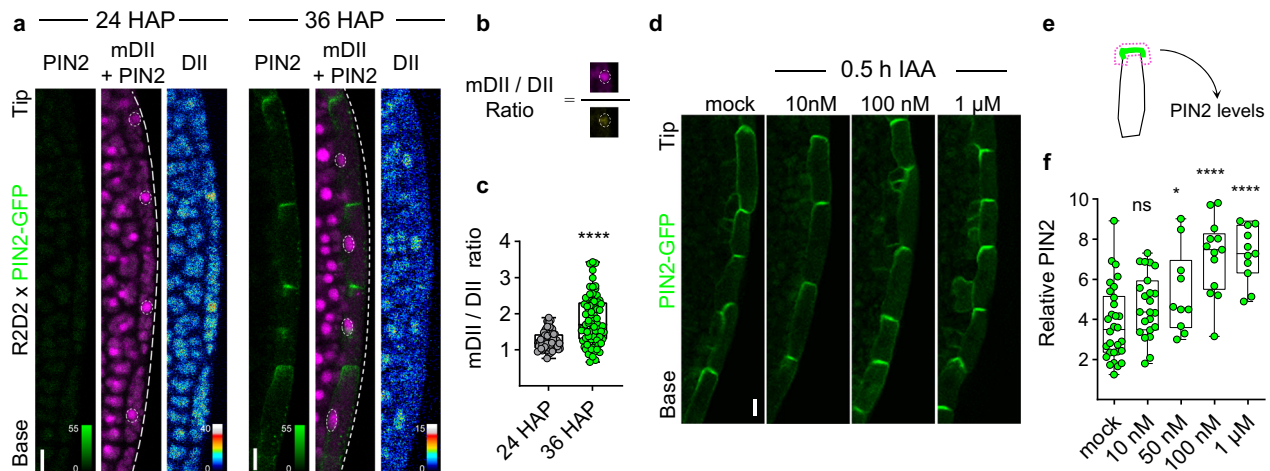


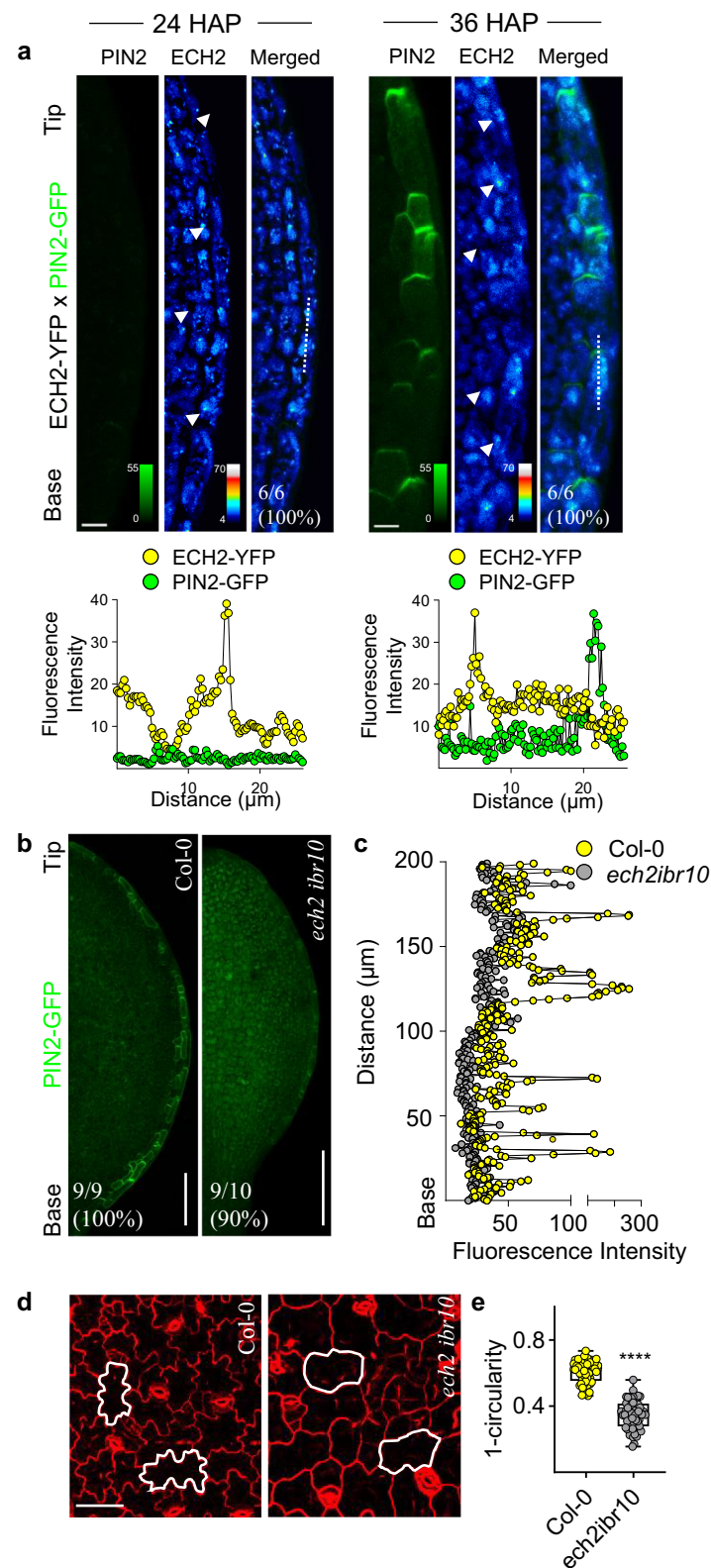
**Fig. 2 | Auxin promotes its own PIN2-mediated efflux along MCs.** **a** Auxin levels increase after PIN2 levels increase. PIN2-GFP +/+ X R2D2 +/- cotyledon's borders at 24 and 36 hours after plating (HAP). R2D2 signal results from DII-Venus (DII) and mDII-ntTomato (mDII). Scale bar = 10  $\mu$ m. PIN2-GFP can only be observed on margin cells (MCs) at 36 but not at 24 HAP. **b** Schematic of quantification of auxin levels using R2D2 in marginal cells (MCs). Nuclear signal intensity from the non-degradable mDII-ntTomato (mDII) is divided by the signal from the auxin-degradable DII-Venus (DII). **c**, Quantification of R2D2 signal according to the formula in **(b)**. Higher mDII/DII ratio indicates higher auxin response. ( $n = 64$  and 75 cells for 24 and 36 HAP, respectively). Data was obtained from 6 cotyledons in each timepoint. Box plot shows all points, the box indicates the 25<sup>th</sup> and 75<sup>th</sup> percentile and the median value, the whiskers indicate minimum and maximum values.

Unpaired two-tailed *t*-test with Welch's correction. \*\*\*\*  $p$ -value < 0.0001. **d** PIN2-GFP-expressing marginal cells (MCs) of 48 HAP cotyledons after 30 min treatment with mock or auxin IAA at the indicated concentrations. Scale bar = 10  $\mu$ m. **e** Red dashed lines indicate the shape of regions used for quantification in **(f)**. **f** Quantification of apical PIN2-GFP after 30 min of auxin IAA treatment. The mean integrated density obtained in the apical side from MCs is normalized by the background fluorescence. Box plot shows all points, the box indicates the 25<sup>th</sup> and 75<sup>th</sup> percentile and the median value, the whiskers indicate minimum and maximum values. ( $n = 30, 23, 10, 13, 11$  cell files for mock, 10 nM, 50 nM, 100 nM and 1  $\mu$ M IAA, respectively). Unpaired two-tailed *t*-test.  $p$ -value = 0.0631 for mock vs 10 nM IAA,  $p$ -value = 0.0319 for mock vs 50 nM IAA, ns  $p$ -value > 0.05, \*  $p$ -value < 0.01, \*\*\*\*  $p$ -value < 0.0001.

pathways, respectively. GFP-TAA1 does not accumulate in MCs prior to PIN2-GFP accumulation (Supplementary Fig. 4a), suggesting the IPyA pathway does not initially trigger PIN2 accumulation. Furthermore, transcripts coding for enzymes working in the IPyA pathway (TAA1, TAR2 and YUC1-11) are weakly or not expressed, while those for the IBA pathway (IBR1, IBR3, IBR10, ECH2) are highly expressed at this developmental stage (Supplementary Fig. 4c, d). However, GFP-TAA1 did accumulate in MCs and epidermal cells after PIN2-GFP was already accumulated (48 HAP), suggesting that the IPyA pathway may work in reinforcing auxin levels (Supplementary Fig. 4a, **white arrows**). In fact, chemical inhibition of the IPyA pathway reduced the accumulated PIN2 levels by ~25% but did not inhibit the formation of the PIN2-based 'pipeline' along MCs (Supplementary Fig. 4e, f).

In contrast, YFP-ECH2 showed clear accumulation in MCs prior to the PIN2 establishment (Fig. 3a) and a clear additional accumulation at the cotyledon tip after PIN2 establishment (Supplementary Fig. 4b).

ECH2-labeled punctate structures could indicate peroxisomal localization (Fig. 3a, **white arrows and intensity profiles**), as shown previously in roots<sup>30</sup>. In peroxisomes, IBA is converted to IAA<sup>30</sup>. This punctate localization of ECH2 in MCs suggests the biosynthesis of IBA-derived IAA in those cells. Thus, we anticipated that PIN2 establishment along MCs would be compromised in IBA-to-IAA conversion mutants. Indeed, *ech2ibr10* showed decreased levels of apical PIN2-GFP in cotyledon MCs at 48 HAP (Fig. 3b, c). Consistent with reduced auxin maxima, *ech2ibr10* cotyledons were smaller and hyponastic (Supplementary Fig. 4g) and exhibited defects in PC interdigitation, as reported previously<sup>2,30</sup> (Fig. 3 d, e). Disrupted auxin transport through the cotyledon margins would explain the reduced *DR5::GUS* expression previously observed in the tip of *ech2ibr10* cotyledons, whose severe PC interdigitation defects were rescued by exogenous auxin<sup>2</sup>. Altogether, these results support the hypothesis that predominantly IBA-to-IAA conversion drives the onset of PIN2 accumulation along MCs,



resulting in the formation of the tip auxin maximum that spatio-temporally coordinates PC interdigitation<sup>2</sup>.

### The distribution of TOB1 to the tonoplast is associated with PIN2 downregulation

The fact that the apical PIN2 levels were greatly reduced in the *ech2ibr10* mutant prompted us to hypothesize that the PIN2 down-

regulation observed around 60-72 HAP in wild type cotyledon MCs (Fig. 1d) may result from a reduction in the IBA-to-IAA conversion in those cells. One possible mechanism for this reduction would be through down-regulation of cytoplasmic IBA availability. Recently, TOB1 was described to reduce the IBA pool by importing IBA into vacuoles, consequently altering lateral root formation<sup>24</sup>. Thus, TOB1 might also regulate IBA availability in cotyledon's MCs, considering

**Fig. 3 | IBA-derived auxin regulates PIN2 accumulation along cotyledons margin cells.** **a** Upper panel, ECH2 expression precedes PIN2. ECH2-YFP +/+ X PIN2-GFP +/+ cotyledons were imaged in the absence and presence of PIN2-GFP at 24 at 36 HAP, respectively. YFP-ECH2 (white arrowhead) is present at 24 HAP, before PIN2 accumulation. Phenotype frequency is shown as a percentage of the number of cotyledons observed. Scale bar = 20  $\mu$ m. Similar results were obtained in 3 independent experiments. Lower panel, Quantification of the signal intensity along the dashed line in the upper panel. **b** IBA-derived auxin is critical for PIN2 accumulation at MCs. PIN2-GFP from cotyledons of wild type *Col-0* and *ech2ibr10*<sup>-/-</sup> grown for 48 hours after root protrusion. Phenotype frequency is shown as a

percentage of the number of cotyledons observed. Similar results were obtained in 3 independent experiments. Scale bar = 100  $\mu$ m. **c** Quantification of PIN2-GFP signal along cotyledons borders of *wt Col-0* (gray) and *ech2ibr10* (yellow) captured from base to tip. **d** IBA-derived auxin is critical for interdigitation. Pavement cells of 5 days-old cotyledons stained with propidium iodide (PI) to outline the cell borders of wild type *Col-0* and double mutant *ech2ibr10*<sup>-/-</sup>. Scale bar = 100  $\mu$ m. **e** Quantification of pavement cell shape (Circularity) in wild type and *ech2ibr10*<sup>-/-</sup> cotyledons, as shown in (d). *n* = 60 cells. Data was collected from 6 different cotyledons on each treatment. Unpaired two-tailed *t*-test. \*\*\*\* *p*-value < 0.0001.

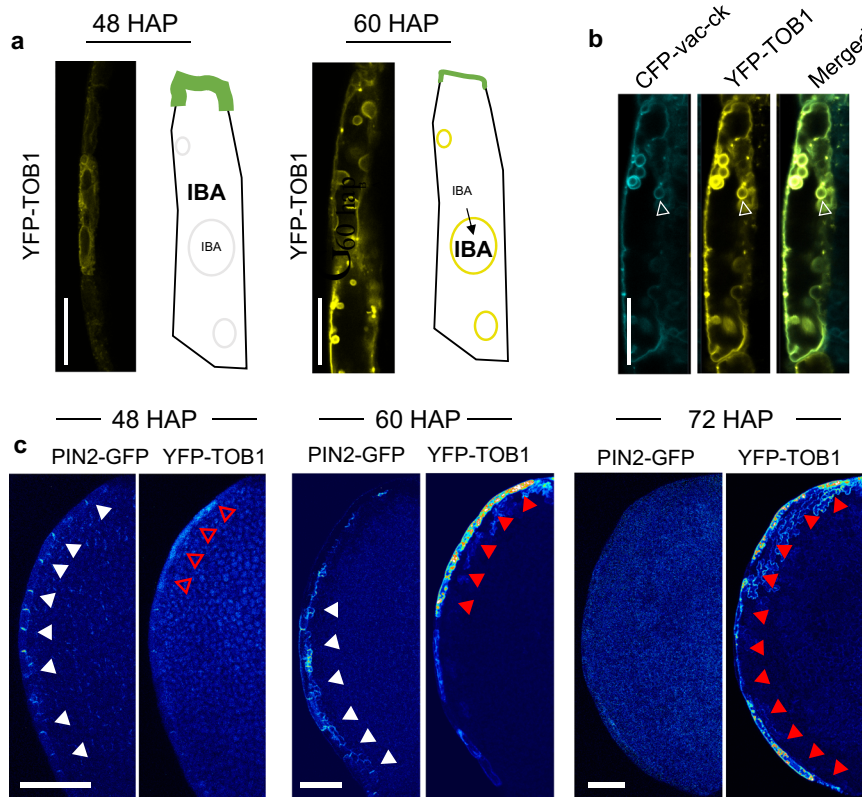


**Fig. 4 | TOB1-mediated vacuole internalization of IBA terminates with PIN2 polar accumulation at cotyledon's marginal cells.** **a** TOB1 consolidates its tonoplast localization in MCs overtime. TOB1::YFP-TOB1 (YFP-TOB1) reticular signal at 48 hours after plating (HAP) changes to tonoplast (ring-like) signal at 60 HAP. To the right of each micrograph, a schematic shows the relationship between PIN2 and TOB1 protein levels. At 48 HAP, PIN2-GFP is abundantly expressed whereas TOB1 displays weak reticular expression pattern. At 60 HAP, PIN2-GFP levels are substantially lower and TOB1 shows clear tonoplast accumulation. Similar results were observed in 4 independent experiments. The complete time course analysis from 24 to 96 HAP can be found in Supplementary Fig. 5. Scale bar size =

20  $\mu$ m. **b** Tonoplast marker CFP-*vac-ck* signal co-localize with YFP-TOB1 signal in 60 HAP cotyledon's MCs. White empty arrowhead indicates the superimposition of CFP-*vac-ck* with YFP-TOB1 signal. Similar results were observed in 3 independent experiments. Scale bar size = 10  $\mu$ m. **c** TOB1 and PIN2 accumulation pattern are inversely correlated. Spectral confocal microscopy image of PIN2-GFP +/+ X YFP-TOB1 +/+ cotyledons grown for 48, 60, 72 hours after plating (HAP). White arrowheads indicate the progressive disappearance of PIN2-GFP signal. Empty red arrowheads denote the reticular YFP-TOB1 expression. Red arrowheads indicate the progressive appearance of tonoplast YFP-TOB1 signal. Similar results were observed in 5 independent experiments. Scale bar size = 100  $\mu$ m.

that TOB1 and PIN2 expression patterns are very similar in shoots, both being expressed in epidermal cells in a highly specific fashion (Supplementary Fig. 5a). In fact, the translational reporter *TOB1p::YFP-TOB1* line (hereafter YFP-TOB1) showed highly specific TOB1 protein accumulation at the cotyledon's MCs during the first 4 days of seedling growth, with some additional expression in neighboring cells (Supplementary Fig. 5c). Notably, the pattern of YFP-TOB1 subcellular distribution changes during cotyledon growth probably reflecting a change in the TOB1 function. YFP-TOB1 signal became reticular when PIN2 accumulation peaked (Fig. 4a, 48 HAP), whereas it was mainly vacuolar/prevacuolar (ring-like) when PIN2 disappeared (Fig. 4a, 60 HAP). Importantly, we found YFP-TOB1 co-localized with the tonoplast marker protein CFP-Vac-ck marker<sup>37</sup> (Fig. 4b) and the tonoplast marker dye FM4-64<sup>38</sup>, surrounding the vacuole lumen marker dye BCECF<sup>39</sup>

(Supplementary Fig. 5b), similar to the observations in roots<sup>24</sup>. Therefore, we propose that tonoplastic TOB1 in MCs sequesters IBA into vacuoles and thus functions to terminate PIN2 accumulation to the apical PM of MCs.

#### Vacuolar IBA importer TOB1 functions to downregulate PIN2 levels in cotyledons

If TOB1 functions to terminate PIN2 accumulation, then its accumulation is expected to correlate with PIN2 accumulation/disappearance spatiotemporal patterns. Thus, we imaged cotyledons expressing translational reporters for both PIN2-GFP (*PIN2p::PIN2-GFP*) and YFP-TOB1 (*TOB1p::YFP-TOB1*) before, during and after PIN2 accumulation in MCs. YFP/GFP signal was accurately separated by means of spectral microscopy<sup>40</sup>. We found TOB1 signal showed progressive tip-to-base

accumulation along the cotyledon's margin while PIN2 signal disappears in the same direction (Fig. 4c, **white vs red arrows**). Although we presumed this is part of a continuous process, we noted 3 discrete stages. First, YFP-TOB1 showed weak signal near the cotyledons tip while PIN2-GFP was highly accumulated along the entirety of the MCs file (Fig. 4c, **48 HAP**). Second, at 60 HAP, YFP-TOB1 consolidated into a ring-like subcellular signal close to the cotyledon tip, while PIN2-GFP disappeared at the tip but remained at the base (Fig. 4c, **60 HAP**). Last, PIN2-GFP was depleted from MCs, whereas YFP-TOB1 was strongly accumulated, opposite to what was found 24 h earlier (Fig. 4c, **72 HAP**). These results indicate that PIN2 and TOB1 accumulate in MCs in an opposing manner.

Next, we tested if TOB1 is functionally required to downregulate PIN2 by introgressing PIN2-GFP into two loss-of-function alleles, *toB1-1* and *toB1-3* (Supplementary Fig. 7a). Both point (*toB1-1*) and insertional mutation (*toB1-3*) increased cotyledon surface areas (Supplementary Fig. 6a). Additionally, both *toB1* mutants showed more expanded epidermal cells when compared to equivalent wild-type cotyledons (Supplementary Fig. 6b–d). As expected, absence of TOB1 causes a 25–30% increase in PIN2 levels in 60 HAP cotyledons (Fig. 5a) and also a delayed PIN2 downregulation observed at 72 HAP (Supplementary Fig. 6e). To test the biological significance of this increment on PIN2 levels, we evaluated the auxin response distribution pattern as reflected with *DR5::GUS* expression. In both *toB1* alleles, *DR5::GUS* signal was enhanced at the tip and at the edges compared to *Col-0* wild type (Fig. 5c). Increased *DR5::GUS* signal in *toB1* was indicative of increased upwards auxin transport and reflecting the inability to prevent IBA to IAA conversion by IBA vacuole storage (red dashed lines and arrowheads in Fig. 5c). Interestingly, in root tips the PIN2-GFP levels remain unaltered in *toB1-1* and *toB1-3* mutants (Supplementary Fig. 7b, c). Additionally, we did not find evidence for genetic interaction between TOB1 and PIN2 for controlling root gravitropism, as *toB1-1 eir1-1* double mutant shows a similar agravitropic response as *eir1-1* mutant (Supplementary Fig. 7d–e). Consistent with these findings, we found that TOB1 and PIN2 are not accumulated in the same cell type in roots (Supplementary Fig. 7f), further corroborating the notion that the TOB1 regulation of PIN2 levels is a cell-autonomous phenomenon. Thus, our results showed that in cotyledons but not in roots TOB1 functions to downregulate PIN2 levels most likely by sequestering IBA into vacuoles and consequently reducing cytoplasmic IAA levels.

### Auxin feedback regulates TOB1 expression

The accumulation of TOB1 in the tonoplast (60 HAP) occurs after PIN2-mediated auxin flow throughout the MCs has started (24–36 HAP). Thus, we hypothesized that once auxin accumulates to relatively high levels it regulates TOB1 expression to terminate PIN2-mediated auxin transport. To test this, we treated cotyledons with incipient TOB1 levels (at 24 HAP) with 100 nM IAA for 4 h. Exogenously applied auxin resulted in a ~30% increment in TOB1 levels (Fig. 5e, f). Under auxin treatments, YFP-TOB1 levels increased along the entire margin (white arrowhead Fig. 5e) but were much higher in those cells closer to the tip (red arrows). This finding is consistent with the above-described tip-to-base wave in the expression of YFP-TOB1 (Fig. 4d, **red arrowheads**). In silico analysis of the *TOB1* promoter revealed several auxin-related motifs, listing ARF7, ARF8, and mARF34 (ARF7/ARF19 paralog in maize) with high confidence in two different algorithms (Supplementary Fig. 7a). These observations suggest auxin may induce *TOB1* expression directly, in addition to cytokinin, a well-known *TOB1* regulator<sup>24</sup>. Alternatively, auxin may regulate *TOB1* gene expression indirectly through auxin-cytokinin interaction. Altogether, we propose that PIN2-transported auxin self-terminates PIN2 expression and auxin transport toward the cotyledon tip by activating the accumulation of TOB1, which further sequesters IBA into vacuoles.

## Discussion

In general, the developmental program of an organism encompasses a continuum of discrete phases, and therefore relies on transient cell-surface signals, transient intracellular signaling structures<sup>41,42</sup> and transient cellular arrangements<sup>43</sup>. Here we show that a transient self-organizing PIN2-based auxin flow takes place in the cotyledon's margin cells, contributing to the cotyledon's tip auxin maxima and the PC interdigitation. In leaf, PIN1, PIN3, PIN4, and PIN7 function in vasculature development independently from PIN2<sup>44</sup>. Future research needs to demonstrate whether PIN2 establishes tip auxin maxima independently or collaboratively with other PINs.

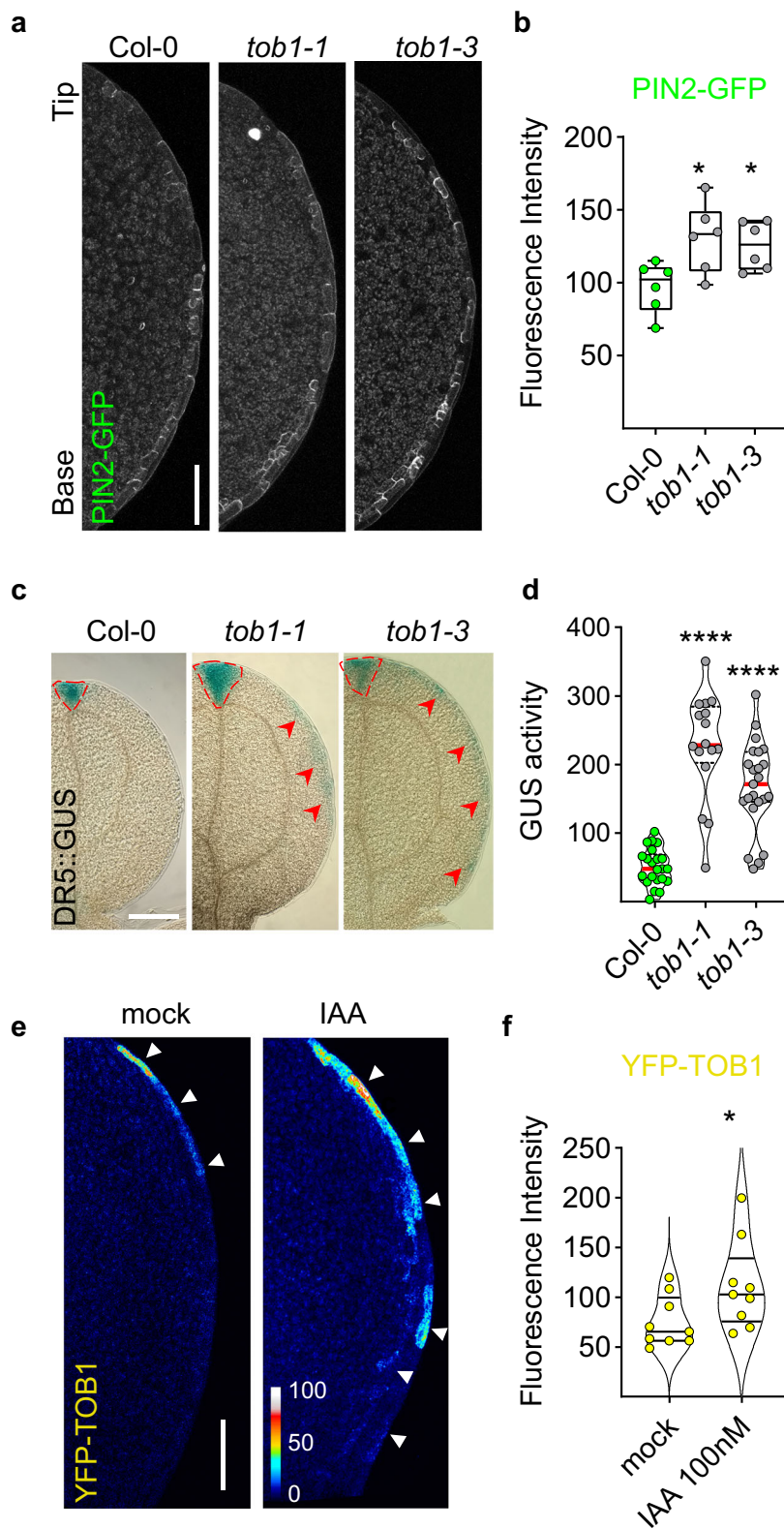
Self-organizing transient signals, similar to the one described here, may be instrumental during different developmental transitions in plants and animals. Besides leaf development, auxin-related self-organizing transient signals may be involved in phyllotaxis<sup>45</sup>, root elongation, and root branching by regulating the cell proliferation to differentiation transition<sup>46</sup>, or in the transition to rapid hypocotyl elongation during germination<sup>47</sup>. In animals, self-organized transient signals might control the circumferential actin filament bundles during the embryo to elongated worm transition in *C. elegans*<sup>48</sup> or the formation of the multicellular rosettes in the epithelial-mesenchymal transition (EMT) during mammalian embryo development<sup>49</sup> or mesenchymal invasion during cancer metastasis<sup>50</sup>.

Remarkably, this transient auxin flow is generated and dismantled within a 48-hour time frame by positive and negative feedback loops, respectively. First, the transient auxin flow is self-promoted by turning-on PIN2 accumulation through the biosynthesis of IBA-derived auxin. Subsequently, the local high auxin at the tip generated by the auxin flow induces TOB1 expression, which import IBA into vacuoles, terminating PIN2 accumulation (Fig. 6). This self-organizing mechanism secures a pulse of auxin flow towards the cotyledon tip, and thus our findings uncover an exciting mechanism for the generation of transient developmental signals.

Our findings also raise some interesting questions about auxin synthesis, auxin flows, and signaling during developmental transitions. First, what is the advantage of employing IBA over other IAA sources? We showed the IBA-to-IAA pathway has a predominant role in MCs and gene expression indicates a preference for this pathway in the entire matured embryo. Early development and expansion of the matured embryo is fueled through fatty acid  $\beta$ -oxidation, a process similar to IBA-to-IAA conversion<sup>51</sup>. Thus, the pathway for auxin synthesis may be tightly linked to the seedling energy sources. Future studies could be directed at determining if and how auxin synthesis pathway preferences switch once seedlings become autotrophic. Second, what is the initial signal that activates the IBA-dependent auxin biosynthesis? The signal must be intrinsic as it is produced during seed imbibition. It could be a mechanical signal resulting from increasing turgor pressure and/or initial cotyledon expansion. Third, what is the signal establishing apical PIN2 polarity along MCs? Different options can be considered; a pre-established tissue-wide polarity field<sup>52,53</sup>, a combination of gene expression waves<sup>54,55</sup> and positive auxin feedback<sup>56,57</sup>, or a nested self-organizing system between localization and auxin flow, as subjected by PIN1 during PC morphogenesis<sup>4,58,59</sup>. In fact, PINs are transiently auxin-induced<sup>60</sup> and present during leaf serration<sup>53,61</sup>.

Leaf borders, in particular leaf serration, have been found critical for the evolution of leaf shape diversity<sup>53,61</sup>. As we have observed polar PIN2 in cotyledons, it would be interesting to decipher if the PIN2-based auxin transient flow and its contribution to PC morphogenesis could work as a link between PC shape diversity<sup>62</sup> and leaf shape diversity<sup>63,64</sup>.

Finally, it is well known that roots and stems show coordinated localization of polar PINs but usually in a multi cell-type context and without a clear start of the process. In contrast, cotyledon PIN2 localization occurs in only one cell type, the marginal cells, and the whole process is activated specifically at 24 HAP, moving auxin tip-wards



throughout 10-15 cells. Thus, we propose that transient auxin flow at MCs might bring an exceptional opportunity to study the mechanisms underlying PIN-based auxin flow.

## Methods

### Plant growth conditions

All plants were grown at 22 °C under a 16 h light/ 8 h dark photoperiod with 85-90  $\mu\text{mol}/\text{s}^2$  of light intensity. In vitro growth was carried out in

0.5X MS basal salt medium with vitamins, 1% sucrose, pH 5.7-5.8 and 0.8% Agar (Sigma-Aldrich® A1296). Hours After Plating (HAP) are counted from the moment the seeds are transferred to the growth conditions after stratification.

### Plant materials

Arabidopsis Columbia (*Col-0*) ecotype is the genetic background for the subsequent lines, including mutants *eir1-1/pin2/CS8058*<sup>32</sup>,

**Fig. 5 | TOB1 regulates PIN2 levels in Arabidopsis cotyledon marginal cells.** **a** PIN2 levels increase in *tob1* mutants. Confocal images of PIN2-GFP cotyledon in *Col-0*, *tob1-1*<sup>-/-</sup> and *tob1-3*<sup>-/-</sup> mutant background, generated by introgression. All lines are non-segregant F3 PIN2-GFP +/+. Images are z-stack maximum projection capturing all detectable fluorescence signal. Scale Bar = 100 μm. **b** Quantification reflecting PIN2-GFP levels in *tob1* mutants. For quantification, a region of interest was defined around the entire file of MCs. Box plot shows all points, the box indicates the 25th and 75th percentile and the median value, the whiskers indicate minimum and maximum values. *n* = 6 cotyledons, 60 HAP. Unpaired two-tailed *t*-test, *p*-value = 0.0185 for *Col-0* vs *tob1-1*, *p*-value = 0.0158 for *Col-0* vs *tob1-3*, \* *p*-value < 0.05. **c** Auxin transcriptional response distribution pattern revealed by DR5-GUS histochemical analysis in 96 HAP cotyledons of wild type, *tob1-1*<sup>-/-</sup> and *tob1-3*

<sup>-/-</sup>. All lines are non-segregant F3 DR5-GUS +/+. Scale bar = 400 μm. **d** GUS activity in cotyledons *tob1-1*<sup>-/-</sup> and *tob1-3*<sup>-/-</sup> measured by fluorometric quantification of 4-MU. GUS activity is shown as nanomolar units of 4-MU per sample. Welch's ANOVA with Dunnett's T3 for multiple comparisons test. \*\*\*\* *p*-value < 0.0001. *n* = 22, 16, 23 samples for *Col-0*, *tob1-1*, *tob1-3*. Sample is defined as the 2 cotyledons in a seedling. **e** Auxin induced TOB1 accumulation. TOB1p::YFP-TOB1 cotyledons grown for 24 HAP were treated during 4 h with mock or 100 nM IAA. Scale bar = 100 μm. **f** Quantification of fluorescence intensity of YFP-TOB1 along the cotyledon's MCs upon auxin treatment. Images are z-stack maximum projection capturing all detectable fluorescence signal. *n* = 9 cotyledons. Unpaired two-tailed *t*-test. *p*-value = 0.0471, \* *p*-value < 0.05.

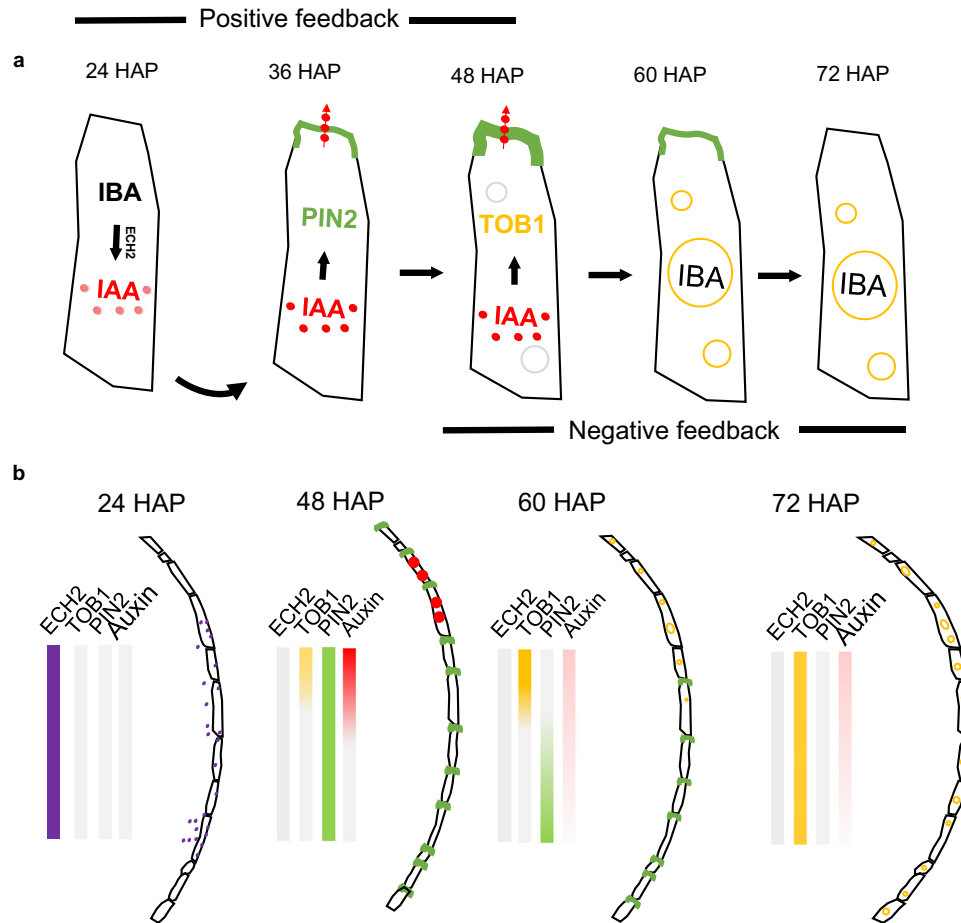


**Fig. 6 | A working model for self-organizing transient auxin flow at cotyledon's margins.** Cotyledon's margins display a transient self-organized PIN2-mediated auxin transport towards the tip. **a** Schematic at a cell level. First, a positive feedback (24-48 HAP) via IBA-derived auxin promotes PIN2 expression and PIN2 apical polar accumulation. Then, a negative feedback (60-72 HAP) is turned on where auxin induces the expression of TOB1 to sequester IBA into vacuoles, reducing IBA-derived auxin and leading to down regulation of PIN2 and cessation of the auxin flow. **b** Schematic at a tissue level. At 24 HAP, ECH2 is accumulated along the margin

(purple) before PIN2 (green), catalyzing IBA-derived auxin (red). PIN2-based auxin transport moves auxin towards the cotyledon tip. At 48 HAP, higher auxin levels at MCs closer to the tip (red gradient upwards) triggers expression of TOB1 (upwards yellow gradient). TOB1 localizes to the tonoplast gradually from tip-to-base. Tonoplast TOB1 reduces IBA-derived auxin, leading to the reduction of PIN2 levels (downwards green gradient). At 72 HAP, the auxin transport system is completely shut down (gray arrow), which coincides with strong tonoplast TOB1 (dark yellow). At this point, a fully interdigitated field of pavement cells is observed.

*pin2-T/SALK\_122916C*<sup>33</sup>, *tob1-3/SALK\_205450*<sup>24</sup>, *tob1-1*<sup>24</sup>, as well as the reporter lines TOB1p::YFP-TOB1<sup>24</sup>, PIN2p::PIN2-GFP<sup>31</sup>, TAA1p::GFP-TAA1<sup>11,36</sup>, 35S::GFP-LTI6b<sup>65</sup>, and CFP-*Vac-ck/CS16256*<sup>37</sup>. R2D2 is in the Columbia-Utrecht ecotype<sup>34</sup>. Dual reporters and reporters in mutant backgrounds were generated by introgression. Upon crossing reporters with a mutant background, homozygous mutations were confirmed in F2, and non-segregating lines for the reporter were obtained by screening several F3 lines. Only non-segregant F3 lines were used throughout the study. Primer sequences and genotyping strategy can be found in Supplementary Table 1.

### Seed sterilization

For experiments analyzing specific developmental time points, seeds were bleach-sterilized as follows: 10 min agitation with 30% bleach in water with 0.1% TX-100 (Triton X-100), followed by rinsing 5 times with sterile water and subsequent stratification for 48 h at 4 °C in dark. Seed sterilization is crucial for the reproducibility of the developmental timepoints described in this manuscript. For routine experiments, sterilization was performed overnight using the vapor-phase method (Clough and Bent, 1998) carried out by simply placing seeds in a desiccator next to a beaker containing 80 mL of

bleach, with 1 mL of concentrated HCl carefully added into the bleach<sup>66</sup>.

### Developmental stages

Using the bleach sterilization protocol and our described plant growing conditions, we observed the following hallmarks in seedling growth: at 0 HAP, a swollen seed coat; at 24 HAP, a longitudinal rupture in the seed coat; at 36 HAP, radicle protrusion but cotyledons remain inside the seed coat; at 48 HAP, cotyledons were greenish and some were covered with their seed coat and root hair-like structures became noticeable at the root-hypocotyl junction; at 60 HAP, green ellipsoidal cotyledons were rarely covered by the seed coat and form a  $\sim 90^\circ$  angle between them; at 72 HAP, green globular-shaped cotyledons were flat with a  $\sim 180^\circ$  angle between them. Hours After Plating (HAP) time is counted from the moment seeds are placed in growing conditions after stratification. Developmental time in *ech2ibr10* mutants was timed as hours after root protrusion, as these mutants showed intrinsic delayed germination.

### Vector construction

The *ECH2* upstream regulatory region was amplified using promECH2-EcoRI, (GAATTCGGTTAGATATAGAAATGACGG) and promECH2-PmlI (CACGTGCCGATCAGGATTAGAGCTCAGC) primers. The resulting 577-bp product, spanning the region between ECH2 and its most upstream neighboring gene, was then cloned into the pCR4 vector (Life Technologies) to create pCR4-ECH2prom. The *ECH2* upstream regulatory region was excised from pCR4-ECH2prom using EcoRI and PmlI enzymes and subcloned into the pMCS:YFP-GW<sup>67</sup> vector to create pECH2:YFP-GW. The *ECH2* cDNA was recombined from pENTR-ECH2<sup>30</sup> into the pECH2:YFP-GW vector using LR Clonase (Life Technologies) to form pECH2::YFP-ECH2, which expresses an N-terminal YFP fusion with ECH2 driven by the *ECH2* upstream regulatory region.

### Imaging and microscopy

Adaxial sides of dissected cotyledons were analyzed. In the early stages of cotyledon development, careful removal of seed coat was necessary to dissect the cotyledon. All images were acquired using laser scanning confocal microscopes (20X objective, NA = 0.75–0.8). Specifically, ablation experiments were performed using either a Leica TCS SP5 or a Leica Stellaris 8 microscope. Linear unmixing was conducted using a Leica TCS SP8 X DLS or a Zeiss 880 microscope. Fluorescent protein (FP) signals were captured using the following settings: propidium iodide (PI; excitation 543/561 nm, emission 580–660 nm), GFP (excitation 488 nm, emission 505–535 nm), and YFP (excitation 488/514 nm, emission 492–530 nm or 520–570 nm, respectively). PC shape analysis was performed with PaCeQuant software as described before<sup>6,68</sup>.

### Linear unmixing

Signal separation of GFP/AF (autofluorescence), GFP/YFP and GFP/PI (propidium iodide) was performed by linear unmixing of spectral images<sup>40</sup> acquired with either the Leica TCS SP8 X DLS, Zeiss LSM 880 Elyra or Zeiss LSM 980 systems, generating identical results. In all cases, reference emission spectra are obtained from samples without mixed signals. For example, in the unmixing of GFP/AF (autofluorescence), a spectrum is obtained from the tip of wild type cotyledons (autofluorescence), while a GFP spectra is obtained from PIN2-GFP signal in the cotyledon's margins of a stable transgenic line.

For the Leica TCS SP8 X DLS, signal separation was performed using lambda mode with a 20X/NA 0.75 objective, excitation with a 488 nm white pulse laser scanning from 490 nm to 630 nm, and detection with HyD detectors. The images were processed using the linear unmixing algorithm in LASX software. For the Zeiss 880, GFP/YFP and GFP/PI signal separation was performed using spectral imaging mode with a 20X/NA 0.8 objective, MBS 488, excitation with a

488 nm argon-ion laser and a 32-channel GaAsP spectral detector capable of simultaneous detection of 8.9 nm bands of signal ranging from 410 nm to 695 nm. For GFP/AF unmixing a Zeiss LSM 980 with 25X/NA 0.8 objective was used in lambda mode, excitation with 488 nm diode laser, and sequential detection with a 4-channel GaAsP spectral detector. For GFP/YFP and GFP/PI separation, we used a detection window of the 16 channels between 490–632, whereas for GFP/AF unmixing, a detection window of 15 channels between 491 nm and 623 was used. The images were processed using the linear unmixing algorithm in Zeiss ZEN software.

### Image analysis

Intensity measurements and circularity [ $4\pi \cdot (\text{area}/\text{perimeter}^2)$ ] were obtained using ImageJ 1.40 (Wayne Rasband, NIH, USA) within a region of interest (ROI) as indicated in each figure legend. Circularity is an isoperimetric quotient, which compares the area of a shape, in our case a pavement cell, against the area of a circle with the same perimeter. Higher circularity values represent less lobing, as they are closer to a circle shape<sup>69</sup>. To observe direct correlation with lobing, we defined interdigitation as 1-circularity. For cell border detection, dissected embryos were incubated either in 100  $\mu\text{g}/\text{mL}$  PI for 10 minutes at room temperature (older cotyledons) or for 10 minutes at 4°C with 5  $\mu\text{M}$  FM4-64 (younger cotyledons) prior to imaging. For apical PIN2-GFP abundance, we quantified the fluorescence at the apical region and normalized it against the background signal. For PIN2-GFP protein polarity, we quantified the fluorescence intensity at the apical side relative to a region of similar area at the middle of the lateral side for each MC. Similar results were obtained regardless of whether the lateral side was located closer to the tip or the base. The fluorescence intensity was obtained in Fiji as the integrated density from z-stack maximum projection confocal images. Both apical and lateral intensities were normalized against the average intensity of 3 randomly selected ROIs in the background.

### GUS (beta-glucuronidase) activity assays

GUS staining assays using X-gluc as a substrate, also known as histological assays, were performed with slight modifications based on previous reports<sup>70,71</sup>. In brief, plant samples were fixed in cold 80% acetone for at least 2 h, which could be extended overnight. Subsequently, they were vacuum infiltrated with the GUS solution for 10 min and incubated in the dark at 37°C for 0.5 h. The GUS solution was prepared as described previously<sup>70</sup>. Alternatively, 2–4 h incubation was necessary without vacuum infiltration. After staining, cotyledons were “cleared” in 70% ethanol with agitation overnight to remove the chlorophyll. Finally, cotyledons were dissected and observed under a light microscope.

GUS activity assays in intact plant tissue with 4-MUG as a substrate, also known as fluorometric assay, were performed with adaptations from previous reports<sup>72,73</sup>. Samples (a pair of cotyledons) were incubated in 96-well microplates (one sample per well) containing 150  $\mu\text{L}$  lysis buffer (50 mM sodium phosphate, pH 7.0, 10 mM EDTA, 0.1% Triton X-100). As suggested in the referenced literature, the entirety of the sample tissue must be completely submerged in the buffer for substrate penetration. Subsequently, 1 mM 4-MUG was added to initiate the reaction, which was then incubated at 37°C for 90 min before being terminated with 50  $\mu\text{L}$  of 0.2 M  $\text{Na}_2\text{CO}_3$ . The substrate 4-MUG is converted to the fluorescence product, 4-MU. To measure 4-MU fluorescence intensity, a multi-mode plate reader SpectraMax iD5 was used under the following specific wavelengths; 365 nm for excitation and 455 nm for emission. A standard curve generated with 4-MU (in lysis buffer plus stop solution) corroborated linearity ( $R^2 = 0.99$ ) for this assay under our experimental conditions within the range of 10 nM to 1000 nM of 4-MU. GUS activity is expressed as nanomolar units of 4-MU per sample.

### Chemical treatments

Exogenous treatments with IAA (100 nM, EtOH) were performed by directly diluting them in liquid growth media without phytoagar. To inhibit the IPyA auxin-biosynthetic pathway, a two-chemical cocktail containing 50  $\mu$ M Yucasin and 10  $\mu$ M L-Kyneurin was used to ensure maximum inhibitory activity<sup>74</sup>. Stock solutions for Yucasin (10 mM, DMSO) and L-Kyneurin (50 mM, DMSO) were directly diluted in the growth medium before plating. At 24 HAP, seedlings were transferred and incubated for 12 h. in the presence of the chemicals. For vacuole markers, seedlings at 60 HAP were treated with 5  $\mu$ M FM4-64 for 10 min and 10  $\mu$ M BCECF-AM for 1 h in darkness. After incubation samples were washed for 30 sec before mounting for observation. FM4-64 (Stock of 10 mM, DMSO) and BCECF (Stock of 10 mM, DMSO) were directly diluted in liquid growth medium without agar.

### Laser ablation

Seedlings of 35S::GFP-LTI6b<sup>65</sup> at 48 HAP were incubated with 100  $\mu$ g/mL with Propidium Iodide (PI) in a microscope slide. A UV 405 nm pulsed laser (300  $\mu$ W power) at 100% laser intensity was used for cell ablation in a Leica SP5 confocal system or Leica Stellaris 8. For LeicaSP5, each cell was irradiated for 5 sec in maximum optical zoom. PI penetrating the cell borders and marking the nuclei demarcated successful ablation. The whole file of marginal cells was ablated within 2-3 minutes. For Stellaris 8, a small window at maximum optical zoom was assigned to each MCs and a sequential irradiation was initiated using the multi-acquisition mode. After ablation, seedlings were re-incubated in vitro in the same growing conditions for further analysis after 24 hours. Vasculature patterns were observed by mounting the mock and ablated samples in Image-IT™ Plant Tissue Clearing Reagent (Invitrogen, V11328).

### In silico analysis

The sequence spanning from +1346 bp until transcription start site (TSS) of the TOB1 gene (ATIG72140) was analyzed using promoter analysis tool PlantRegMap. Additionally, the sequence extending +1000 bp upstream the TSS was examined using PSCAN, <http://159.149.160.88/pscan>, a widely used promoter analysis tool. The PINs and TAA/YUCCA gene expression analysis was obtained from published data<sup>75,76</sup> by submitting gene codes to Arabidopsis ePlant browser <http://bar.utoronto.ca/eplant>. Cell-type specific expression analysis data for PIN2, TOB1 was obtained from translatoME data at <http://efp.ucr.edu>.

### Statistical methods

All statistical analyses were performed using GraphPad Prism®. An unpaired two-samples two-tailed *t*-test, or a two-way ANOVA with Šídák's test for multiple comparisons was used throughout the study, with a 95% confidence interval. Equal variance was assumed for the *t*-test and assessed with a post F-test. Unequal variances were subject to a Welch's *t*-test or a Welch's ANOVA with a Dunnett's T3 multiple comparisons test. Statistical significance was defined as follows: ns (no significance) *p*-value > 0.05, \* *p*-value < 0.05, \*\* *p*-value < 0.01, \*\*\* *p*-value < 0.001, \*\*\*\* *p*-value < 0.0001.

### Reporting summary

Further information on research design is available in the Nature Portfolio Reporting Summary linked to this article.

### Data availability

All data underlying this study are available from the corresponding author upon request. Source data are provided with this paper for the main and the Supplementary Figs. Gene accession numbers involved in this study: PIN2 = AT5G57090 and TOB1 = ATIG72140. Source data are provided with this paper.

### References

1. Fu, Y., Gu, Y., Zheng, Z., Wasteneys, G. & Yang, Z. Arabidopsis interdigitating cell growth requires two antagonistic pathways with opposing action on cell morphogenesis. *Cell* **120**, 687–700 (2005).
2. Pérez-Henríquez, P. et al. Hierarchical global and local auxin signals coordinate cellular interdigitation in *Arabidopsis*. *BioRxiv* <https://doi.org/10.1101/2024.06.17.599171>. (2024)
3. Xu, T. et al. Cell surface- and rho GTPase-based auxin signaling controls cellular interdigitation in *Arabidopsis*. *Cell* **143**, 99–110 (2010).
4. Xu, T. et al. Cell surface ABPI-TMK auxin-sensing complex activates ROP GTPase signaling. *Science* **343**, 1025–1028 (2014).
5. Pérez-Henríquez, P. & Yang, Z. Extranuclear auxin signaling: a new insight into auxin's versatility. *New Phytol* **237**, 1115–1121 (2023).
6. Yu, Y. et al. ABLs and TMKs are co-receptors for extracellular auxin. *Cell* **186**, 5457–5471.e17 (2023).
7. Pan, X. et al. Auxin-induced signaling protein nanoclustering contributes to cell polarity formation. *Nat. Commun.* **11**, 3914 (2020).
8. Benková, E. et al. Local, efflux-dependent auxin gradients as a common module for plant organ formation. *Cell* **115**, 591–602 (2003).
9. Sabatini, S. et al. An auxin-dependent distal organizer of pattern and polarity in the *Arabidopsis* root. *Cell* **99**, 463–472 (1999).
10. Friml, J. Fourteen stations of auxin. *Cold Spring Harb. Perspect. Biol.* **14**, a039859 (2022).
11. Tao, Y. et al. Rapid synthesis of auxin via a new tryptophan-dependent pathway is required for shade avoidance in plants. *Cell* **133**, 164–176 (2008).
12. Ljung, K. Auxin metabolism and homeostasis during plant development. *Development* **140**, 943–950 (2013).
13. Casanova-Sáez, R., Mateo-Bonmati, E. & Ljung, K. Auxin metabolism in plants. *Cold Spring Harb. Perspect. Biol.* **13**, (2021).
14. Adamowski, M. & Friml, J. PIN-dependent auxin transport: action, regulation, and evolution. *Plant Cell* **27**, 20–32 (2015).
15. Grieneisen, V. A., Xu, J., Marée, A. F. M., Hogeweg, P. & Scheres, B. Auxin transport is sufficient to generate a maximum and gradient guiding root growth. *Nature* **449**, 1008–1013 (2007).
16. Barbosa, I. C. R., Hammes, U. Z. & Schwechheimer, C. Activation and polarity control of PIN-FORMED auxin transporters by phosphorylation. *Trends Plant Sci* **23**, 523–538 (2018).
17. Péret, B. et al. AUX/LAX genes encode a family of auxin influx transporters that perform distinct functions during *Arabidopsis* development. *Plant Cell* **24**, 2874–2885 (2012).
18. Jenness, M. K., Tayengwa, R. & Murphy, A. S. An ATP-binding cassette transporter, *abcb19*, regulates leaf position and morphology during phototropin1-mediated blue light responses. *Plant Physiol* **184**, 1601–1612 (2020).
19. Jenness, M. K., Carraro, N., Pritchard, C. A. & Murphy, A. S. The *Arabidopsis* atp-binding cassette transporter *abcb21* regulates auxin levels in cotyledons, the root pericycle, and leaves. *Front. Plant Sci.* **10**, 806 (2019).
20. Zhao, Y. Auxin biosynthesis and its role in plant development. *Annu. Rev. Plant Biol.* **61**, 49–64 (2010).
21. Frick, E. M. & Strader, L. C. Roles for IBA-derived auxin in plant development. *J. Exp. Bot.* **69**, 169–177 (2018).
22. Peer, W. A., Cheng, Y. & Murphy, A. S. Evidence of oxidative attenuation of auxin signalling. *J. Exp. Bot.* **64**, 2629–2639 (2013).
23. Mravec, J. et al. Subcellular homeostasis of phytohormone auxin is mediated by the ER-localized PIN5 transporter. *Nature* **459**, 1136–1140 (2009).
24. Michniewicz, M. et al. TRANSPORTER OF IBA1 links auxin and cytokinin to influence root architecture. *Dev. Cell* **50**, 599–609.e4 (2019).
25. Korasick, D. A., Enders, T. A. & Strader, L. C. Auxin biosynthesis and storage forms. *J. Exp. Bot.* **64**, 2541–2555 (2013).

26. Han, X. et al. Auxin-callose-mediated plasmodesmal gating is essential for tropic auxin gradient formation and signaling. *Dev. Cell* **28**, 132–146 (2014).
27. Dubreuil, C., Jin, X., Grönlund, A. & Fischer, U. A local auxin gradient regulates root cap self-renewal and size homeostasis. *Curr. Biol.* **28**, 2581–2587 (2018).
28. Band, L. R. et al. Root gravitropism is regulated by a transient lateral auxin gradient controlled by a tipping-point mechanism. *Proc. Natl Acad. Sci. USA* **109**, 4668–4673 (2012).
29. Zhao, Y. Auxin biosynthesis: a simple two-step pathway converts tryptophan to indole-3-acetic acid in plants. *Mol. Plant* **5**, 334–338 (2012).
30. Strader, L. C. et al. Multiple Facets of Arabidopsis Seedling Development Require Indole-3-Butyric Acid-Derived Auxin. *Plant Cell* **23**, 984–999 (2011).
31. Xu, J. & Scheres, B. Dissection of Arabidopsis ADP-RIBOSYLATION FACTOR 1 function in epidermal cell polarity. *Plant Cell* **17**, 525–536 (2005).
32. Luschnig, C., Gaxiola, R. A., Grisafi, P. & Fink, G. R. EIR1, a root-specific protein involved in auxin transport, is required for gravitropism in Arabidopsis thaliana. *Genes Dev* **12**, 2175–2187 (1998).
33. Zhu, R. et al. Heterotrimeric G Protein-Regulated Ca<sup>2+</sup> Influx and PIN2 Asymmetric Distribution Are Involved in Arabidopsis thaliana Roots' Avoidance Response to Extracellular ATP. *Front. Plant Sci.* **8**, 1522 (2017).
34. Liao, C.-Y. et al. Reporters for sensitive and quantitative measurement of auxin response. *Nat. Methods* **12**, 207–210 (2015). 2 p following 210.
35. Vieten, A. et al. Functional redundancy of PIN proteins is accompanied by auxin-dependent cross-regulation of PIN expression. *Development* **132**, 4521–4531 (2005).
36. Stepanova, A. N. et al. TAA1-mediated auxin biosynthesis is essential for hormone crosstalk and plant development. *Cell* **133**, 177–191 (2008).
37. Nelson, B. K., Cai, X. & Nebenführ, A. A multicolored set of in vivo organelle markers for co-localization studies in Arabidopsis and other plants. *Plant J* **51**, 1126–1136 (2007).
38. Rigal, A., Doyle, S. M. & Robert, S. Live cell imaging of FM4-64, a tool for tracing the endocytic pathways in Arabidopsis root cells. *Methods Mol. Biol.* **1242**, 93–103 (2015).
39. Scheuring, D., Schöller, M., Kleine-Vehn, J. & Löffke, C. Vacuolar staining methods in plant cells. *Methods Mol. Biol.* **1242**, 83–92 (2015).
40. Zimmermann, T., Marrison, J., Hogg, K. & O'Toole, P. Clearing up the signal: spectral imaging and linear unmixing in fluorescence microscopy. *Methods Mol. Biol.* **1075**, 129–148 (2014).
41. Banani, S. F., Lee, H. O., Hyman, A. A. & Rosen, M. K. Biomolecular condensates: organizers of cellular biochemistry. *Nat. Rev. Mol. Cell Biol.* **18**, 285–298 (2017).
42. Sager, R. et al. Auxin-dependent control of a plasmodesmal regulator creates a negative feedback loop modulating lateral root emergence. *Nat. Commun.* **11**, 364 (2020).
43. Harding, M. J., McGraw, H. F. & Nechiporuk, A. The roles and regulation of multicellular rosette structures during morphogenesis. *Development* **141**, 2549–2558 (2014).
44. Verna, C., Ravichandran, S. J., Sawchuk, M. G., Linh, N. M. & Scarpella, E. Coordination of tissue cell polarity by auxin transport and signaling. *eLife* **8**, (2019).
45. Refahi, Y. et al. A stochastic multicellular model identifies biological watermarks from disorders in self-organized patterns of phyllotaxis. *eLife* **5**, (2016).
46. Ishida, T. et al. Auxin modulates the transition from the mitotic cycle to the endocycle in Arabidopsis. *Development* **137**, 63–71 (2010).
47. Bou Daher, F. et al. Anisotropic growth is achieved through the additive mechanical effect of material anisotropy and elastic asymmetry. *eLife* **7**, e38161 (2018).
48. Lardennois, A. et al. An actin-based viscoplastic lock ensures progressive body-axis elongation. *Nature* **573**, 266–270 (2019).
49. Gredler, M. L. & Zallen, J. A. Multicellular rosettes link mesenchymal-epithelial transition to radial intercalation in the mouse axial mesoderm. *Dev. Cell* **58**, 933–950.e5 (2023).
50. Leggett, S. E. et al. Motility-limited aggregation of mammary epithelial cells into fractal-like clusters. *Proc Natl Acad Sci USA* **116**, 17298–17306 (2019).
51. Strader, L. C., Culler, A. H., Cohen, J. D. & Bartel, B. Conversion of endogenous indole-3-butyric acid to indole-3-acetic acid drives cell expansion in Arabidopsis seedlings. *Plant Physiol* **153**, 1577–1586 (2010).
52. Bringmann, M. & Bergmann, D. C. Tissue-wide mechanical forces influence the polarity of stomatal stem cells in Arabidopsis. *Curr. Biol.* **27**, 877–883 (2017).
53. Mansfield, C. et al. Ectopic BASL Reveals Tissue Cell Polarity throughout Leaf Development in Arabidopsis thaliana. *Curr. Biol.* **28**, 2638–2646.e4 (2018).
54. Gould, P. D. et al. Coordination of robust single cell rhythms in the Arabidopsis circadian clock via spatial waves of gene expression. *eLife* **7**, e31700 (2018).
55. Bargmann, B. O. R. et al. A map of cell type-specific auxin responses. *Mol. Syst. Biol.* **9**, 688 (2013).
56. Paciorek, T. et al. Auxin inhibits endocytosis and promotes its own efflux from cells. *Nature* **435**, 1251–1256 (2005).
57. Oochi, A. et al. Pinstatic acid promotes auxin transport by inhibiting PIN internalization. *Plant Physiol* **180**, 1152–1165 (2019).
58. Nagawa, S. et al. ROP GTPase-dependent actin microfilaments promote PIN1 polarization by localized inhibition of clathrin-dependent endocytosis. *PLoS Biol* **10**, e1001299 (2012).
59. Li, H. et al. Phosphorylation switch modulates the interdigitated pattern of PIN1 localization and cell expansion in Arabidopsis leaf epidermis. *Cell Res* **21**, 970–978 (2011).
60. Scarpella, E., Marcos, D., Friml, J. & Berleth, T. Control of leaf vascular patterning by polar auxin transport. *Genes Dev* **20**, 1015–1027 (2006).
61. Runions, A., Tsiantis, M. & Prusinkiewicz, P. A common developmental program can produce diverse leaf shapes. *New Phytologist* **2**, 401–418(2017).
62. Sapala, A. et al. Why plants make puzzle cells, and how their shape emerges. *eLife* **7**, e32794 (2018).
63. Kierzkowski, D. et al. A growth-based framework for leaf shape development and diversity. *Cell* **177**, 1405–1418.e17 (2019).
64. Bilsborough, G. D. et al. Model for the regulation of Arabidopsis thaliana leaf margin development. *Proc Natl Acad Sci USA* **108**, 3424–3429 (2011).
65. Cutler, S. R., Ehrhardt, D. W., Griffiths, J. S. & Somerville, C. R. Random GFP::cDNA fusions enable visualization of subcellular structures in cells of Arabidopsis at a high frequency. *Proc. Natl. Acad. Sci. USA*. **97**, 3718–3723 (2000).
66. Clough, S. J. & Bent, A. F. Floral dip: a simplified method for Agrobacterium-mediated transformation of Arabidopsis thaliana. *Plant J* **16**, 735–743 (1998).
67. Michniewicz, M., Frick, E. M. & Strader, L. C. Gateway-compatible tissue-specific vectors for plant transformation. *BMC Res. Notes* **8**, 63 (2015).
68. Möller, B., Poeschl, Y., Plötner, R. & Bürstenbinder, K. PaCeQuant: a tool for high-throughput quantification of pavement cell shape characteristics. *Plant Physiol* **175**, 998–1017 (2017).
69. Andriankaja, M. et al. Exit from proliferation during leaf development in Arabidopsis thaliana: a not-so-gradual process. *Dev. Cell* **22**, 64–78 (2012).
70. Jefferson, R. A., Kavanagh, T. A. & Bevan, M. W. GUS fusions: beta-glucuronidase as a sensitive and versatile gene fusion marker in higher plants. *EMBO J* **6**, 3901–3907 (1987).

71. Jefferson, R. A. The GUS reporter gene system. *Nature* **342**, 837–838 (1989).
72. Blázquez, M. Quantitative GUS activity assay in intact plant tissue. *CSH Protoc.* **2007**, pdb.prot4688 (2007).
73. Halder, V. & Kombrink, E. Facile high-throughput forward chemical genetic screening by in situ monitoring of glucuronidase-based reporter gene expression in *Arabidopsis thaliana*. *Front. Plant Sci.* **6**, 13 (2015).
74. Nishimura, T. et al. Yucasin is a potent inhibitor of YUCCA, a key enzyme in auxin biosynthesis. *Plant J* **77**, 352–366 (2014).
75. Nakabayashi, K., Okamoto, M., Koshihara, T., Kamiya, Y. & Nambara, E. Genome-wide profiling of stored mRNA in *Arabidopsis thaliana* seed germination: epigenetic and genetic regulation of transcription in seed. *Plant J* **41**, 697–709 (2005).
76. Klepikova, A. V., Kasianov, A. S., Gerasimov, E. S., Logacheva, M. D. & Penin, A. A. A high resolution map of the *Arabidopsis thaliana* developmental transcriptome based on RNA-seq profiling. *Plant J* **88**, 1058–1070 (2016).

## Acknowledgements

We acknowledge David Carter at UCR Microscopy Core for technical assistance with Zeiss 880 microscopy, Lei Shi at FAFU-UCR center for technical assistance with Leica SP8 microscopy, and Olivier Brun for technical assistance with Leica Stellaris 8. We are thankful to Dr. Yi Tao for providing published material, TAA1p::GFP-TAA1. This work was in part supported by the National Institute of General Medical Sciences to Z.Y. (GM081451), the National Science Foundation to X.C. and Z.Y. (1853698) and the National Natural Science Foundation of China Grants to Z.Y. (3241101698).

## Author contributions

P.P.-H. carried out most of the experiments; Z.Y. and P.P.-H. interpreted the results and designed experiments. M.M. cloned constructs for TOB1 and ECH2 supervised by L.S. X.C. helped with statistical analysis. J.V.N. co-supervised P.P.-H. during the revision of this manuscript. S.N, W.T, X.P, Z.L, C.R., and J.V.N. contributed critical skills in microscopy. P.P.-H. and Z.Y. wrote the manuscript. All authors commented on the manuscript.

## Competing interests

The authors declare no competing interests.

## Additional information

**Supplementary information** The online version contains supplementary material available at <https://doi.org/10.1038/s41467-024-55480-8>.

**Correspondence** and requests for materials should be addressed to Zhenbiao Yang.

**Peer review information** *Nature Communications* thanks the anonymous reviewers for their contribution to the peer review of this work. A peer review file is available.

**Reprints and permissions information** is available at <http://www.nature.com/reprints>

**Publisher's note** Springer Nature remains neutral with regard to jurisdictional claims in published maps and institutional affiliations.

**Open Access** This article is licensed under a Creative Commons Attribution-NonCommercial-NoDerivatives 4.0 International License, which permits any non-commercial use, sharing, distribution and reproduction in any medium or format, as long as you give appropriate credit to the original author(s) and the source, provide a link to the Creative Commons licence, and indicate if you modified the licensed material. You do not have permission under this licence to share adapted material derived from this article or parts of it. The images or other third party material in this article are included in the article's Creative Commons licence, unless indicated otherwise in a credit line to the material. If material is not included in the article's Creative Commons licence and your intended use is not permitted by statutory regulation or exceeds the permitted use, you will need to obtain permission directly from the copyright holder. To view a copy of this licence, visit <http://creativecommons.org/licenses/by-nc-nd/4.0/>.

© The Author(s) 2025